The Journal of Chemical Physics

Mercury-indium-sulfide nanocrystals: A new member of the family of ternary in based chalcogenides

Cite as: J. Chem. Phys. **151**, 144701 (2019); https://doi.org/10.1063/1.5119991
Submitted: 16 July 2019 . Accepted: 16 September 2019 . Published Online: 08 October 2019

Oleksandr Stroyuk, Alexandra Raevskaya, Felix Spranger, Oleksandr Selyshchev, Volodymyr Dzhagan, Dmytro Solonenko, Nikolai Gaponik, Dietrich R. T. Zahn, and Alexander Eychmüller

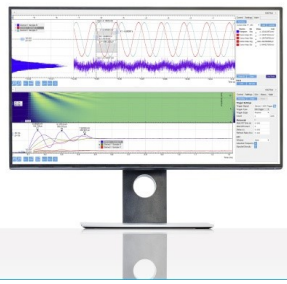

The Journal of Chemical Physics ARTICLE scitation.org/journal/jcp

Mercury-indium-sulfide nanocrystals: A new member of the family of ternary in based chalcogenides

Cite as: J. Chem. Phys. 151, 144701 (2019); doi: 10.1063/1.5119991
Submitted: 16 July 2019 • Accepted: 16 September 2019 •
Published Online: 8 October 2019

Oleksandr Stroyuk,[1,2,a)] Alexandra Raevskaya,[2] Felix Spranger,[3] Oleksandr Selyshchev,[4] Volodymyr Dzhagan,[5,6] Dmytro Solonenko,[4] Nikolai Gaponik,[3] Dietrich R. T. Zahn,[4] and Alexander Eychmüller[3,a)]

AFFILIATIONS

[1]Forschungszentrum Jülich GmbH, Helmholtz-Institut Erlangen Nürnberg für Erneuerbare Energien (HI ERN), Immerwahrstr. 2, 91058 Erlangen, Germany
[2]L.V. Pysarzhevsky Institute of Physical Chemistry, National Academy of Sciences of Ukraine, Kyiv 03028, Ukraine
[3]Physical Chemistry, TU Dresden, 01062 Dresden, Germany
[4]Semiconductor Physics, Chemnitz University of Technology, 09107 Chemnitz, Germany
[5]V. Lashkaryov Institute of Semiconductor Physics, National Academy of Sciences of Ukraine, Kyiv 03028, Ukraine
[6]Taras Shevchenko National University of Kyiv, 01601 Kyiv, Ukraine

Note: This paper is part of the JCP Special Topic on Colloidal Quantum Dots.
[a)]**Authors to whom correspondence should be addressed:** o.stroyuk@fz-juelich.de; alstroyuk@ukr.net; and alexander.eychmueller@chemie.tu-dresden.de

ABSTRACT

A general synthesis approach of aqueous glutathione-capped ternary Ag–In–S, Cu–In–S, and Hg–In–S nanocrystals (NCs) is introduced, allowing the NC composition to be varied in a broad range. Ternary Hg–In–S (HIS) NCs are reported for the first time and found to have the same tetragonal chalcopyrite motif as Cu–In–S and Ag–In–S NCs, corroborated by phonon spectra, while X-ray photoelectron spectroscopic data indicate mercury to be present as Hg^+ in the Hg–In–S NCs. Colloidal HIS and Hg–In–S/ZnS NCs showed little or no variations of the spectral width of the photoluminescence band upon NC size selection, temperature variation in a broad range of 10–350 K, deposition of a ZnS shell, or postsynthesis annealing. All these observations are similar to those reported earlier for Ag–In–S and Ag–In–S/ZnS NCs and allowed us to assume a general photoluminescence mechanism for all three ternary compounds, based on the model of radiative self-trapped exciton recombination.

I. INTRODUCTION

Luminescent ternary metal-chalcogenide nanocrystals (NCs) or quantum dots, such as copper or silver indium sulfide/selenide, have emerged recently as a viable alternative to the more conventional binary cadmium or lead chalcogenide NCs for various optoelectronic and sensing applications.[1–10] The ternary NCs feature strong absorption of visible light and intense photoluminescence (PL) with PL quantum yields (QYs) higher than 60%, emitted in broad bands located in the visible and near infrared (NIR) parts of a spectrum.[1–5,7–10] The spectral characteristics of absorption and PL bands can be varied in a broad range by changing both the NC composition and the size as well as by alloying with zinc sulfide and other chalcogenides. The highest PL efficiencies as well as photochemical activities are typically observed for the nonstoichiometric Cu–In–S (CIS) and Ag–In–S (AIS) compounds depleted with respect to the monovalent cation (Cu^+ or Ag^+).[1,3–5,7–10] At the same time, the nature and mechanisms of the broadband PL of In-based ternary compounds, both in the bulk and nanocrystalline forms, still remain among the controversially debated issues.[3,5,8] In particular,

comparative studies of CIS- and AIS-based compounds showed that both copper and silver ions can act as hole-localizing centers despite the fact that Ag^+ is more persistent to oxidation than Cu^+. To account for these results, a new model for the hole-localizing centers was suggested assuming that holes are accommodated by AgX or CuX (X = S, Se) octahedra, resulting in a NC lattice distortion and strong vibrational contributions to the PL emission.[3,5,11] In this view, further studies of other possible ternary compounds, in particular, with metals capable of changing the oxidation state from +1 to +2, are expected to considerably contribute to a better understanding of the general mechanisms of photoexcitation and radiative recombination in ternary metal chalcogenides.

In the present paper, we introduce a new member of the "family" of nonstoichiometric ternary In-based sulfides—mercury indium sulfide Hg–In–S (HIS) NCs as well as core/shell HIS/ZnS NCs stabilized in aqueous solutions by biocompatible multifunctional glutathione (GSH). We present a general aqueous synthetic pathway to all three ternary compounds and focus on the discussion of similarities and differences of the spectral properties of these compounds.

II. MATERIALS AND METHODS

Aqueous colloidal core AIS, CIS, and HIS NCs were synthesized in de-ionized (DI) water in a reaction between a mixture of Ag(I), Cu(II), Hg(II), and In(III) complexes with glutathione (GSH) and sodium sulfide followed by a thermal treatment at 96–98 °C similarly to our previous reports.[12,13] A ZnS shell was then deposited on core AIS, CIS, or HIS NCs by the decomposition of Zn(II)-GSH complexes in the presence of core NCs at 96–98 °C. Details of the synthesis procedures are presented in the supplementary material.

NCs were characterized by absorption and photoluminescence (PL) spectroscopy, Raman and infrared (IR) spectroscopies, X-ray diffraction (XRD), inductively coupled optical emission spectroscopy (ICP-OES), atomic force microcopy (AFM), and X-ray photoelectron spectroscopy (XPS). The spectroscopic measurements and characterization were performed for core and core/shell NCs synthesized at the nominal ratios M:In:S = 1.5:8:10 and M:Zn = 1:10. The experimental details on the measurements and sample preparations can be found in the supplementary material.

III. RESULTS AND DISCUSSION

A. Composition-dependent optical properties of HIS and HIS/ZnS NCs

Glutathione is a multifunctional ligand providing several functionalities for the formation of chelate complexes with metal ions both in the free form and on the surface of metal chalcogenide NCs. A broad range of binary chalcogenide NCs was reported to be stabilized with GSH directly in aqueous solutions or transferred to water via a ligand exchange, as discussed by us in detail in Ref. 12. GSH was found to be a robust and versatile ligand to stabilize colloidal aqueous CIS-[14–17] and AIS-based[18–20] NCs. Recently, we also reported the aqueous syntheses of colloidal AIS and AIS/ZnS NCs capped with GSH.[12,13]

Here, we extend the latter synthetic approach to form colloidal ternary Hg–In–S NCs stabilized by GSH as well as a combination of a surface ZnS shell and GSH ligands. The synthesis is highly reproducible and is based on the interaction between sodium sulfide and a combination of GSH complexes with Hg(II), In(III), and Zn(II) in hot (96°–98°) alkaline aqueous solutions. We should also note that, along with GSH, HIS and HIS/ZnS NCs can also be capped with smaller multifunctional ligands such as thioglycolic acid, mercaptopropionic acid, and cysteine, similar to AIS and AIS/ZnS NCs studied by us earlier.[21,22] The spectral properties of composition- and size-selected HIS and HIS/ZnS NCs capped with these different multifunctional ligands were found to be very similar, but the GSH-capped NCs showed the highest stability and resistance to air oxidation at prolonged storage. In this view, we focused our present study on the GSH-capped mercury-indium-sulfide NCs.

The as-produced NCs can be precipitated by ethanol or 2-propanol, separated from unreacted complexes and redispersed to concentrated colloids, retaining stability toward aggregation and oxidation for many months. Alternatively, the crude HIS (HIS/ZnS) can be subjected to a size-selected precipitation using 2-propanol as a nonsolvent similarly as reported by us for AIS and AIS/ZnS NCs[12,21,22] and resolved into a series of fractions with different average sizes and optical properties.

An increase in the nominal (set at the synthesis) Hg-to-In ratio results in an increase of the total absorbance of the final colloidal GSH-capped HIS NCs [Fig. 1(a)] in an almost linear proportion to the mercury content [inset in Fig. 1(a), curve 1]. A qualitatively similar situation is observed for the core/shell HIS/ZnS NCs [supplementary material, Fig. S1(a)]. The absorption spectra of HIS (HIS/ZnS) NCs are characterized by a distinct maximum at around 450 nm (2.7–2.8 eV) and a longer-wavelength tail extending into the NIR range [Fig. 1(a)]. In every case, a clear absorption edge can be observed after the conversion of the spectral curves using the Tauc equation for the case of direct allowed electronic transitions [supplementary material, Fig. S2(a)], allowing the bandgap to be estimated for a given Hg-to-In ratio. The bandgap of HIS NCs was found to decrease monotonously from 2.74 eV for Hg-poor NCs [Fig. 1(a), inset, curve 2 and supplementary material, Table S1] to 2.45 eV for the HIS NCs with the highest mercury content probed in the present work (nominal Hg-to-In ratio of 3/8). Similarly, the bandgap of the core/shell HgS/ZnS NCs decreases from 2.85 eV for Hg/In = 0.5/8 to 2.66 eV for Hg/In = 3/8 (supplementary material, Table S1). Taking the thioglycolic acid-capped HIS/ZnS NCs as an example, we showed that the colloidal solutions produced at a different nominal [Hg]/[In] ratio (from 0.063 to 0.375) have a similar average hydrodynamic size ranging from 4 to 4.5 nm (supplementary material, Fig. S3). Therefore, we can exclude a possible size effect on the variation of the spectral properties observed for HIS (HIS/ZnS) NCs with different mercury-to-indium ratios.

To assess the real Hg content in the composition-selected HIS NCs, we determined the atomic composition of a set of samples with a nominal [Hg]/[In] ratio of 0, 0.063, 0.188, 0.25, 0.375, and 1.0 using energy-dispersive X-ray spectroscopy (supplementary material, Table S2). The real [Hg]/[In] ratios found were 0, 0.11, 0.22, 0.32, 0.42, and 1.1, respectively. The values are higher than the nominal ratios, most probably due to a partial removal of In^{III} in the

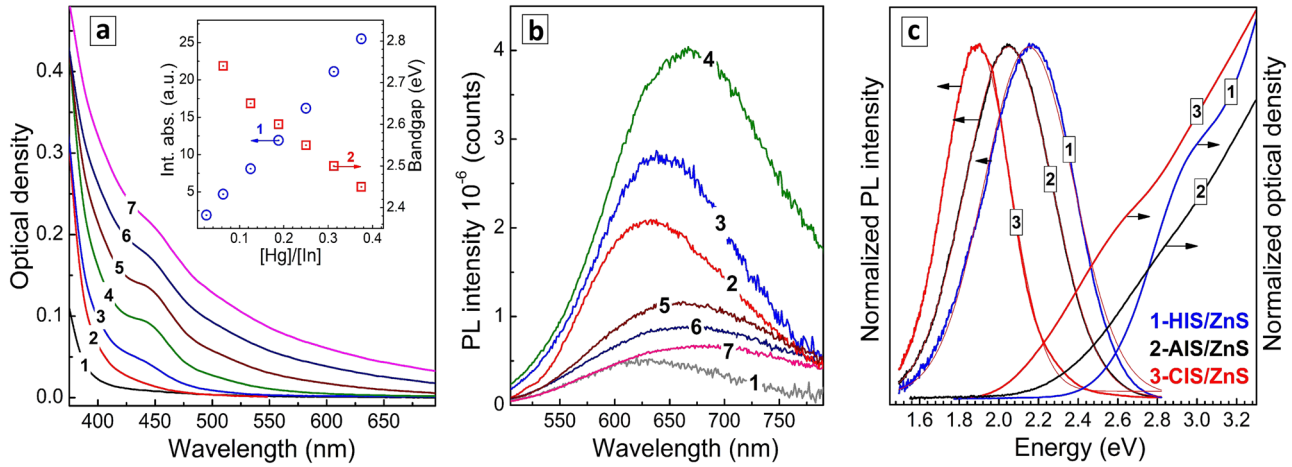

FIG. 1. Absorption (a) and PL (b) spectra of colloidal HIS-GSH NCs synthesized at different molar mercury-to-indium ratios [Hg]/[In] = 0.025 (curve 1), 0.063 (curve 2), 0.125 (curve 3), 0.188 (curve 4), 0.250 (curve 5), 0.313 (curve 6), and 0.375 (curve 7). Inset in (a): integral absorption of colloidal HIS-GSH measured in the range of $h\nu$ = 1.77–3.18 eV (curve 1) and NC bandgap (curve 2) as functions of the NC composition. (c) Normalized absorption spectra (left section) and PL spectra (right section) of aqueous colloidal HIS/ZnS NCs (curves 1), AIS/ZnS NCs (curves 2), and CIS/ZnS NCs (curves 3).

form of complexes with the ligand on the purification step and an enrichment of the NCs with mercury relative to the nominal content. There exists a linear correlation between the nominal and the real [Hg]/[In] ratios (supplementary material, Fig. S4), showing that the real composition of HIS NCs follows the nominal composition set during the synthesis.

The dependence of absorption on the mercury content is very similar to the same dependence reported by us earlier both for CIS[23] and AIS NCs[12,21,24] where a linear proportionality on the Cu or Ag content was observed for the entire range of the compositions studied. These results allow concluding that for all three cases the light absorption centers are clearly associated with the M^+ ion (Ag^+, Cu^+, or Hg^+) of the NC lattice, indicating a general mechanism of the interband electronic transitions.

The absorption "tail" of GSH-capped HIS and HIS/ZnS NCs, that is, the absorbance with energies lower than the bandgap, can be linearized in the coordinates of the Urbach equation [supplementary material, Fig. S2(b)], and the characteristic Urbach energy E_U can be determined from the slopes of the corresponding curves. The Urbach energy characterizes the degree of the NC lattice disorder and increases from ≈200 meV for Hg-poor NCs to beyond 500 meV for Hg-rich NCs (supplementary material, Table S1). It should be noted that E_U remains roughly constant at Hg/In ratios lower than ≈0.2, and then, it increases sharply for Hg-richer compositions, indicating a much higher disorder. Similar tendencies were also observed for core/shell HIS/ZnS NCs, showing that the passivation of the HIS core with a ZnS shell affects surface defects of the NCs (resulting in a PL increase as discussed below) but does not alter the internal structure of the HIS cores.

The PL of HIS and HIS/ZnS NCs is emitted in broad bands with large Stokes shifts and a composition-dependent position of the band maximum [Fig. 1(b); supplementary material, Fig. S1(b)]. No PL emission is observed for pure GSH-capped indium sulfide species. The PL intensity (normalized to the absorption at the PL excitation wavelength) was found to increase from the Hg-poor compositions, reaching a maximum at a nominal ratio of Hg/In = 1.5/8, and then decrease for compositions enriched with mercury [Fig. 1(b)]. The nominally stoichiometric $HgInS_2$ NCs exhibit a negligibly low PL QY. The decrease of the PL efficiency for the compositions with Hg/In ratios larger than ≈0.2 correlates with the sharp increase in the Urbach energy discussed above, indicating that the internal disorder is likely to be responsible for the loss of the efficiency of the radiative recombination.

The core HIS and core/shell HIS/ZnS NCs with a nominal Hg-to-In ratio of 1.5/8 exhibiting the highest PL QY were selected for further in-depth characterization and comparison with AIS- and CIS-based NCs prepared at the same nominal Ag-to-In and Cu-to-In ratios. Figure 1(c) shows that the HIS/ZnS NCs exhibit the largest bandgap (the shortest wavelength of the absorption edge) of all three compounds, while the PL is emitted in broad and symmetrical bands irrespective of the core composition. The PL band maximum follows the bandgap and shifts from 2.16 eV for HIS/ZnS to 2.05 eV for AIS/ZnS NCs and to 1.89 eV for CIS/ZnS NCs (Table I). The spectral width of the PL bands (or FWHM) was found to be large for all three compositions, decreasing from 440 to 450 meV for HIS/ZnS and AIS/ZnS to 335 meV for CIS/ZnS NCs. The highest PL QY of around 50% was observed for AIS/ZnS NCs, while CIS/ZnS and HIS/ZnS exhibit lower PL efficiencies and QYs of 18% and 7%, respectively (Table I).

Earlier, we discussed the special features of the broadband PL of AIS and AIS/ZnS NCs both in ensembles[12,21] and on the single-particle level[13] and showed that the most probable origin of the broadband emission of such ternary NCs is the self-trapped exciton recombination. In this model, one of the charge carriers gets localized on certain sites of the lattice, resulting in a strong electron-phonon interaction and a considerable contribution of the phonon replicas to the emission spectrum being the reason of large PL

TABLE I. Comparison of the PL parameters of aqueous GSH-capped CIS/ZnS, AIS/ZnS, and HIS/ZnS NCs of the same nominal composition. Note: the experimentally determined errors are ±1%, ±0.01 eV, and ±5 meV for the PL QY, PL max, and PL FWHM, respectively.

NC composition	PL QY (%)	PL max (eV)	PL FWHM (meV)
CIS/ZnS	18	1.89	335
AIS/ZnS	50	2.05	440
HIS/ZnS	7	2.16	450

FWHMs. Below, we show that HIS and especially HIS/ZnS NCs reveal a similar PL behavior with broad PL bands and no distinct contributions from the NC size and trap energy distributions to the PL FWHMs.

B. Characterization of the structure, composition, and morphology of ternary NCs

1. XRD measurements

The X-ray diffraction patterns of HIS NCs resemble strongly those of GSH-capped AIS and CIS NCs [Fig. 2(a)], showing the structural identity of the three compounds. The diffractograms of AIS and CIS NCs show a set of three strongly broadened reflections typical for tetragonal chalcopyrite that can be indexed as (112), (220), and (312) planes (JCPDS card Nos. 25-1330 and 27-0159 for AIS and CIS, respectively). The most intense (112) reflection shifts from 27.8° for CIS to 27.0° for AIS, indicating a lattice expansion due to the larger ionic radius of Ag^+ (1.22 Å for the coordination number 6[25]), as compared to Cu^+ (0.77 Å[25]). The (112) reflection of HIS (27.4°) can be found in between the corresponding reflections of AIS and CIS due to the intermediary ionic radius of Hg^+ (1.19 Å for the coordination number 6[25]). The deposition of a ZnS shell results in a decrease of the lattice parameters and in corresponding shifts of the reflection positions, indicating doping of the core materials with Zn^{2+} ions. The most intense (112) peaks can be found at 27.4° for AIS/ZnS, 27.9° for HIS/ZnS, and 28.0° for CIS/ZnS [Fig. 2(b)].

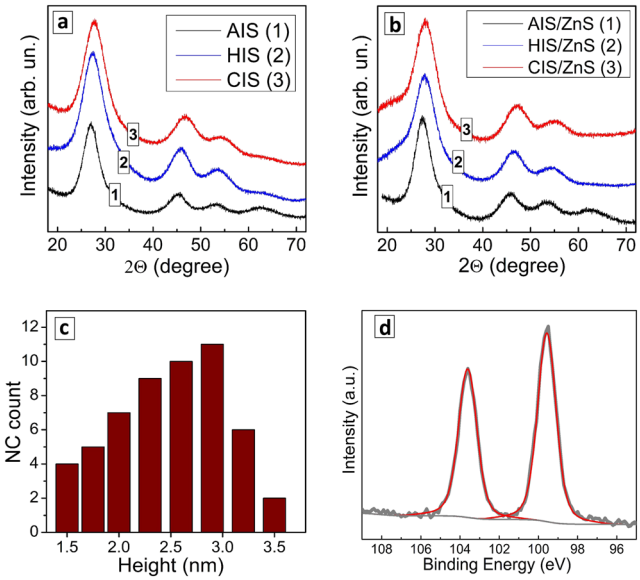

FIG. 2. [(a) and (b)] XRD profiles of core AIS, HIS, and CIS NCs (a) and core/shell AIS/ZnS, HIS/ZnS, and CIS/ZnS NCs (b); (c) size distribution of HIS/ZnS NCs derived from AFM images; (d) high-resolution X-ray photoelectron spectrum in the range of the Hg 4f electron binding energies.

Strong broadening of the reflections indicates a very small size of the NCs of AIS, HIS, and CIS, which was estimated using the Scherrer equation to be around 2.5 nm for the AIS-based NCs and ≈2 nm for the CIS- and HIS-based ones (supplementary material, Table S3). However, these values should be regarded only as an evaluation in view of the structural disordering of the HIS and HIS/ZnS NCs reflected optically in rather high values of the Urbach energy. The core and core/shell NCs show very similar values of the size of the coherent X-ray diffraction domains, indicating that the thickness of the (outer) pure ZnS shell is too thin to appear in the XRD data. Below, we discuss the results of resonant (UV) Raman spectroscopy applied for this purpose.

The XRD measurements of freshly prepared and aged HIS/ZnS NCs attest to their perfect long-term stability. The XRD pattern of both samples has the same structure (peak position and FWHM) for the freshly prepared HIS/ZnS colloid and for a same sample stored in dark under ambient conditions for 11 months (supplementary material, Fig. S5). This indicates that no Ostwald ripening or phase transition takes place during the prolonged shelf-storage of the HIS/ZnS colloids.

It should be noted that the synthesis and properties of tetragonal HIS and compounds based thereon were to our knowledge not reported before either as bulk crystals or as colloidal NCs. The only reports found on the mercury-indium-chalcogenide systems concern spinel $HgIn_2S_4$ based on mercury(II).[26–30]

2. ICP-OES measurements

ICP-OES of core AIS, HIS, and CIS NCs dissolved in HNO_3 showed the following ratios of metals in core NCs: Ag:In = 1:3.0, Cu:In = 1:2.8, Hg:In = 1:2.6. As the original ratios of metal (Ag, Cu, Hg) to indium set during the synthesis were 1:4, a portion of In(III) can be assumed to remain unreacted in the form of In(III) complexes with GSH, which are then separated from the NCs during the precipitation/redispersion procedures. We should note that the nominal ratio of 1:4 produced the highest PL QY for AIS and AIS/ZnS, while for HIS (HIS/ZnS) the highest emission efficiency is observed at a smaller Hg content corresponding to the nominal [Hg]/[In] ratio of 1.5:8. To enable comparisons between AIS, CIS, and HIS compounds, we therefore use the nominal metal(I)-to-indium ratio of 1:4 for all three compounds in the ICP-OES experiments.

The metal ratios in core/shell NCs were found to be Ag:In:Zn = 1:3.0:7.0, Hg:In:Zn = 1:2.8:7.5, and Cu:In:Zn = 1:2.5:6.0. The nominal metal (Ag, Cu, Hg) to zinc ratios were set as 1:10 during the synthesis and, similar to In, we can assume that a portion of Zn(II) is not transformed into ZnS and remains in the form of Zn-GSH complexes in solution.

3. AFM

Similar to the earlier studied CIS/ZnS and AIS/ZnS NCs, the HIS/ZnS NCs strongly tend to agglomerate when deposited onto carbon/copper substrates for transmission electron microscopy (TEM), resulting in unresolved NC aggregates observed in the TEM images (see examples in the supplementary material, Fig. S6). To directly assess the size of NCs additionally to the above-discussed XRD results, we studied very diluted NCs deposited onto mica substrates using AFM. The HIS/ZnS NCs were observed as clearly distinguishable objects with a relatively regular height of 2–3 nm (supplementary material, Fig. S7). Figure 1(c) displays a height distribution chart confirming that the average NC size is around 2.5–3.0 nm, which is close to the XRD-derived estimations. A shift of the distribution toward larger values, as compared to the XRD results, can be assumed to originate from the relatively thick GSH shell around the NCs.

4. X-ray photoelectron spectroscopy

Survey spectra of the colloidal core/shell AIS (HIS, CIS) NCs show the presence of Ag (Hg, Cu), Zn, In, and sulfur from the lattice and ligands as well as carbon, nitrogen, and oxygen from the surface ligand shell. We reported earlier that high-resolution XPS spectra of the Ag 3d range of core and core/shell GSH-capped AIS/ZnS NCs[12] as well as the Cu 3d range of mercaptoacetate-capped CIS/ZnS NCs[23] showed the typical features of silver and copper present in the oxidation state +1. Here, we have additionally tested GSH-capped CIS/ZnS NCs to find out the valence state of copper in these NCs.

The Cu 2p electron binding energy range of the XPS spectrum of GSH-capped CIS NCs shows a doublet of peaks at 931.8/951.7 eV [supplementary material, Fig. S8(a)] with a splitting of 19.9 eV. Both the peak positions and the doublet splitting are characteristic for the Cu(I) state of copper.[31,32] Also, the absence of additional features at ≈934/954 eV as well as of satellite peaks of Cu(II) species at ≈940–945 eV indicate that here copper is present in the CIS-GSH sample most exclusively as copper(I). So, in both AIS/ZnS and CIS/ZnS NCs, the silver and copper ions are in the oxidation state +1 expected for the tetragonal chalcopyrites. As the GSH-capped HIS/ZnS NCs show the same XRD pattern, we can expect Hg also to be present as Hg^+ because the rarely reported mercury(II)-indium chalcogenides crystallize in lattices of different symmetries.[26,27,33] The XPS spectrum in the range of the Hg 4f electron binding energy [Fig. 2(d)] shows a doublet at 99.6 eV ($4f_{7/2}$) and 103.6 eV ($4f_{5/2}$) with a characteristic splitting of 4 eV. Available data on the electron binding energies of mercury and its compounds are relatively scarce and show a strong overlap of values reported for Hg^0, Hg^+, and Hg^{2+}. For example, metallic mercury was reported to show the $4f_{7/2}$ peak at 99.7–99.9 eV,[34] while HgS revealed a characteristic peak at 100.0–101.0 eV, depending on the conductivity of the samples.[35,36]

No data on Hg^+ in compounds with sulfide could be found. The majority of XPS reference data on salts of Hg^+ showing $4f_{7/5}$ peaks at 101.1–101.2 eV come from a sole source[37] and cannot be verified. So, the presence of Hg^+ in the HIS compound discussed here cannot be proven as directly as Cu^+ in CIS. The Hg 4f spectrum fits to one doublet (FWHM 1.15 eV), which indicates one oxidation state of mercury in the sample. At the same time, the range of 4f electron binding energies typical for Hg^{2+} is quite far from the peak presented in Fig. 2(d). Therefore, we can conclude that Hg^{2+} is absent in the studied HIS/ZnS sample or is present only as a negligible contribution in accordance with the previously discussed XRD data.

For both HIS and HIS/ZnS NCs, the range of the In 3d electron binding energies reveals a doublet at 444.6 and 452.1 eV with the position and splitting (7.5 eV) characteristic of In^{3+} in indium sulfide[32] and in the ternary CIS compound.[38] The Zn 2p range contains doublet peaks at 1021.5 and 1044.5 eV with a doublet splitting of 23 eV characteristic of Zn^{2+}.

The S 2p electron binding energy spectrum can be deconvoluted into a combination of three doublets at 161.3/162.5 eV, 162.2/163.4 eV, and 167.8/169.0 eV with a characteristic doublet splitting of 1.2 eV [supplementary material, Fig. S8(b)]. The first two are typical for thiol-capped metal-sulfide NCs and can be assigned to lattice sulfur and surface-bound thiol moieties, respectively. The third doublet is typical for oxidized forms of sulfur, SO_x,[31] and indicates the partial surface oxidation of GSH-capped HIS and CIS NCs. No such signal was observed previously for mercaptoacetate- and GSH-capped AIS (AIS/ZnS) NCs,[12,21] indicating that the presence of these species depends on the M^+ metal in ternary NCs. Taking into account the reported capability of copper sulfide and other copper-containing species for the catalytic oxidation of sulfide (hydrosulfide) ions,[39,40] which was also observed for mercury sulfide NCs,[40] we may assume that the GSH-capped CIS and HIS NCs undergo a partial surface oxidation due to the catalytic properties of Cu^+ (Hg^+) ions in the process of sulfide oxidation by air oxygen.

The C1 range reveals three peaks at 284.8 eV, 285.9 eV, and 288.0 eV [supplementary material, Fig. S8(c)] assigned to aliphatic carbon in $-CH_2-$ groups, C–OH, and COOH groups of GSH, respectively. The N1 electron binding energy range shows two peaks at 399.9 and 401.3 eV [supplementary material, Fig. S8(d)] that can be assigned to amine/amide species in GSH in consistence with the presence of amine and amide nitrogen atoms in the GSH ligand.

C. PL properties of HIS and HIS/ZnS NCs with optimal composition

1. Influence of shell deposition and postsynthesis heating

The deposition of a protective shell (such as ZnS for metal chalcogenide NCs) and a postsynthesis thermal treatment are the two most common methods of improving the efficiency of the radiative electron-hole recombination in semiconductor NCs. We found both of these methods to be very efficient when applied to aqueous AIS NCs[12,21,24] and CIS NCs,[23] resulting in much higher PL QY and prolonged stability toward oxidation and aggregation. Earlier, we showed that probably the most striking feature of both the ZnS shell deposition and the postsynthesis heating of GSH-capped AIS/ZnS colloids is that the strong enhancement of the PL QY is not accompanied by any appreciable changes of the spectral width of the PL bands.[13] These facts indicate that defects present in the volume and on the surface of AIS NCs do not govern the radiative events in the AIS/ZnS NCs because otherwise both treatments would invariably change the density and energy distribution of the defect sites

and affect the final distribution of the PL energies. Such insensitivity of the PL FWHM to the ZnS shell deposition and to the postsynthesis annealing is also observed in the present case of HIS/ZnS NCs.

As discussed above, the deposition of a ZnS shell on the HIS core by thermal decomposition of a Zn(II)-GSH complex results in a strong enhancement of the PL efficiency and a "blue" shift of both the absorption band edge and the position of the PL band maximum [Fig. 3(a)]. The latter shift is a generally reported phenomenon for the In-based ternary NCs originating from the incorporation of Zn^{2+} ions into the lattice of the ternary compounds and the formation of an alloyed structure.[8] The HIS-ZnS alloy is expected to have a higher bandgap as compared to the core HIS NCs. At the same time, the effective size of the HIS core is reduced due to the alloy formation. Both factors can contribute to the increase of the bandgap of core/shell HIS/ZnS NCs, resulting in the "blue" shift of the absorption and PL bands.

Earlier, we reported on Cu-doped AIS NCs[23] where copper dopants occupied the lattice vacancies available in the AIS structure and the deposition of a ZnS shell was not accompanied by the Zn^{2+} penetration into the lattice, thus only resulting in the PL enhancement. This example shows that both phenomena—Zn^{2+} inclusion and PL enhancement—are not necessarily inter-related and the increase of the probability of radiative recombination in AIS NCs upon the deposition of a ZnS shell originates from the passivation of surface defects, as happens in the case of "conventional" binary NCs, such as CdS or CdSe NCs, rather than from the formation of AIS-ZnS alloys.

Therefore, we may expect a considerable suppression of the defect-related radiative recombination as well as narrowing of the defect-related PL after the ZnS shell deposition if we assume the broadband PL to be associated with deeply trapped charge carriers. However, both for AIS/ZnS NCs[12,13] and for the present HIS/ZnS NCs, we observe an opposite trend—the PL enhancement resulting from the ZnS shell deposition is accompanied by a spectral broadening. As shown in Fig. 3(a), the PL intensity of the HIS cores increases by almost a factor of two after the shell deposition. The PL spectra of both HIS and HIS/ZnS NCs can be fitted with a single Gaussian profile, yielding FHWMs of 450 meV for the core HIS and 530 meV for the core/shell HIS/ZnS NCs. As discussed above, the core/shell HIS/ZnS NCs are characterized by a larger Urbach energy, which in combination with the increased FWHM and a change of the lattice parameter observed by XRD shows that the lattice of HIS NCs is disturbed and modified by the inclusion of Zn^{2+} ions. So, we may conclude that the formation of a ZnS shell exerts the opposite effect of distorting the lattice of HIS NCs rather than passivating the existing surface defects. Therefore, the most probable role of the ZnS shell is in the formation of a higher-bandgap interfacial barrier, impeding the electron transfer from the HIS core NCs to the surrounding medium and thus favoring the radiative recombination.

The postsynthesis annealing of colloidal HIS NC solutions at 96–98 °C also results in a considerable enhancement of the PL, which is proportional to the treatment duration at early stages but reaches a saturation at longer times [Fig. 3(b)]. The treatment results also in a slight shift of the absorption band edge and makes the absorption maximum more prominent, both factors indicating a narrowing of the size distribution of the HIS NCs due to the well-known Ostwald ripening process. As summarized by Table S4 in the supplementary material, the annealing results in a decrease of the bandgap from 2.57 to 2.54 eV, a shift of the PL band maximum from 2.09 to 2.05 eV, and an almost 5-fold enhancement of the total PL intensity. At the same time, both the Urbach energy calculated from the absorption spectra and the PL band FWHM remain almost unchanged. These observations indicate that any possible narrowing of the energy distribution of available defect sites induced by the annealing is neither reflected in changes of the absorption "tails" nor in the spectral width of the PL band. Therefore, the defects present in HIS NCs do not strongly affect the dynamics and energetics of the broadband PL emission of HIS NCs, similarly as earlier observed by us for the cases of AIS and AIS/ZnS NCs.[12,13]

2. Absorption and PL properties of HIS (HIS/ZnS) NCs—size-selective fractionation

Earlier, we reported on the feasibility of the size-selective precipitation of a number of fractions from the original colloidal ensemble of AIS and AIS/ZnS NCs capped both by mercaptoacetate[21,22] and GSH.[12,13] We found that the fractions have a distinctly different average size decreasing from 3 to 3.5 nm for the first fractions to 2 nm and less for further fractions, with the total number of fractions reaching 8–10 and more.[12,13] As the AIS and AIS/ZnS NCs of

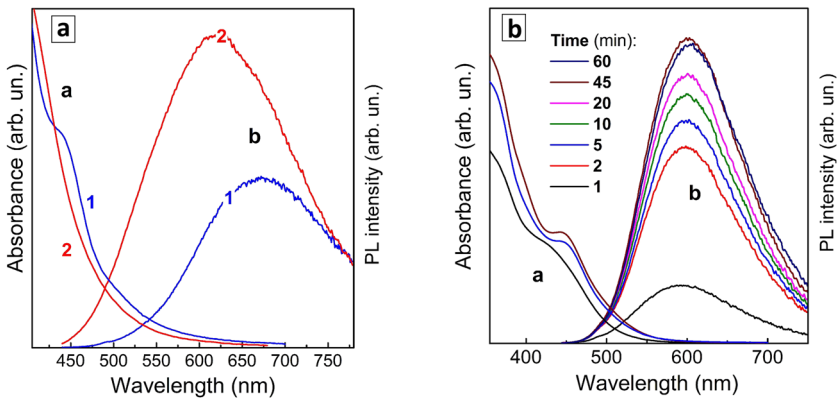

FIG. 3. (a) Absorption spectra (section a) and PL spectra (section b) of core-only GSH-capped HIS NCs (curves 1) and core/shell HIS/ZnS NCs (curves 2) prepared at the same nominal ratio of [Hg]/[In] = 0.188. (b) Absorption spectra (section a) and PL spectra (section b) of colloidal HIS NCs subjected to thermal treatment at 96–98 °C for 1–60 min (see the color coding in the figure).

such sizes exhibit strong spatial exciton confinement, a tiny variation of the average NC size among the fractions results in spectacular changes of the optical properties, in particular, the PL color changing from deep red for the largest NCs to yellow and bluish for the smallest NCs.[12,13] A detailed study of fractionated AIS and AIS/ZnS NCs by XPS showed them to display similar compositions, which infers that size effects are exclusively responsible for the observed spectral changes. Here, we found that a similar size-selection procedure can be applied to GSH-stabilized colloidal ensembles of HIS/ZnS NCs. The results are of preliminary character, and further work is currently under way for the evaluation of the average sizes of HIS/ZnS NCs in separate fractions and correlations between the sizes of the HIS (HIS/ZnS) NCs and their bandgap and PL properties.

In particular, we found that a portion-wise addition of 2-propanol to aqueous GSH-stabilized HIS/ZnS colloids results in the acquisition of several fractions with distinctly different absorption spectra. This is illustrated in Fig. S9 of the supplementary material for HIS/ZnS colloids synthesized with the optimal composition (Hg-to-In ratio of 1.5/8 as discussed above). More than 60 mass% of the original NCs can be found in the first fraction, and the population of the other fractions decreases quite rapidly, leaving less than 1% of the total HIS/ZnS mass in fraction No. 4 [Fig. S9(a)]. This in not particularly encouraging; however, it can be taken as an indication that HIS/ZnS NCs have a much narrower size distribution than the previously studied AIS/ZnS NCs. The latter conclusion is also supported by the presence of a clear maximum in the absorption spectra of the HIS/ZnS NCs [see Figs. 1(a) and 1(c)], which was not observed for AIS/ZnS NCs.[12,13] The absorption edge shifts gradually from ≈480 nm for fraction No. 1 to 450 nm for fraction No. 3 and to less than 400 nm for the last fraction No. 4 [supplementary material, Fig. S9(b)].

The PL band maximum of the fractionated HIS/ZnS NCs also shows a shift from 560 nm (2.22 eV) for the first fraction to 545 nm (2.28 eV) with the FWHM remaining almost constant (around 440 meV) for all four fractions [supplementary material, Fig. S9(c)]. A similar lack of a size effect on the PL band FWHM was observed by us earlier for AIS/ZnS NCs and taken as one of the arguments in favor of the self-trapped excitonic model of the PL emission for such ternary NCs.[12,13]

3. Temperature-dependent PL properties of HIS/ZnS NCs

The PL behavior of HIS and HIS/ZnS NCs was studied in the broad temperature range of 10–350 K using samples that were drop-cast and dried from the concentrated colloidal solutions on glass substrates. Recently, we reported on the temperature dependence of the PL properties of ternary AIS/ZnS NCs produced by similar approaches.[13,41] We found that AIS and AIS/ZnS NCs show tendencies typical for the PL originating from the direct radiative electron-hole recombination such as widely reported for CdS or CdSe NCs. In particular, the PL bands did not show any narrowing and shift with decreasing temperature that can be ascribed to a thermally activated redistribution of trapped charge carriers among the traps of different depths. Additionally, the AIS/ZnS NCs showed some low-temperature features characteristic for the radiative recombination of self-trapped excitons, in particular, a drop of the PL intensity at temperatures lower than 50 K.[42–44] To shed light on the temperature dependences of the PL of the present HIS and HIS/ZnS NCs, we compare them to similar dependences observed for AIS or AIS/ZnS NCs. As core/shell NCs retain a much higher stability toward oxidation under the experimental conditions as well as a generally better reproducibility of the optical characteristics, we mainly discuss the temperature dependences of the PL of core/shell NCs, while the results obtained for core-only HIS and AIS NCs are provided in the supplementary material (Fig. S10).

Both AIS/ZnS and HIS/ZnS NCs show a considerable and monotonous increase in the PL intensity as the temperature is lowered [Fig. 4(a)]. As discussed above, the GSH-capped AIS/ZnS NCs show some drop of the PL intensity at T < 50 K [Fig. 4(a), curve 1] that can be interpreted as the result of the thermal activation of an exciton self-trapping[46] or, alternatively, as the result of a rearrangement of the ligand shell, which is often observed for such NC-ligand systems.[42–44] A similar drop is also observed for the GSH-capped HIS/ZnS NCs, however, a smaller one and at a lower temperature, namely, at T < 25 K [Fig. 4(a), curve 2]. The difference in the threshold temperature of this effect can be interpreted in terms of a smaller activation energy of the transition from the free exciton to a trapped exciton[45] for the HIS/ZnS NCs. The smaller activation energy of the emitting self-trapped exciton state and a higher probability of its nonradiative decay may account for the much lower PL QY of the HIS/ZnS as compared to the AIS/ZnS NCs.

The core-only AIS and HIS NCs [supplementary material, Fig. S10(a)] as well show a general increase of the PL efficiency with decreasing temperature. However, for the core-only NCs, these tendencies are much weaker, especially for the HIS NCs, most probably due to a considerable interference from the defect-related radiative processes competing with the self-trapped exciton emission.

Both AIS/ZnS and HIS/ZnS NCs show very similar temperature dependences of the PL maximum that increases monotonously with a decrease in temperature [Fig. 4(b)]. This is typical for the semiconductor NCs and arises from a "hardening" of the NC lattice and a corresponding increase of the bandgap. While core-only AIS NCs show qualitatively the same temperature dependence as core/shell NCs [supplementary material, Fig. S10(b), curve 1], HIS NCs exhibit a peculiar dependence with the PL band maximum decreasing by ≈100 meV as the temperature is lowered to ≈200 K [supplementary material, Fig. S10(b), curve 2] and then increasing at even lower temperatures. As in the above case of the temperature dependence of the PL intensity, this feature can be assumed to originate from a complex interplay of the self-trapped exciton recombination and radiative processes with the participation of deeply trapped charge carriers with a distribution of depths and detrapping activation energies, as we observed earlier for the deep-trap emission of II-VI NCs.[41,46]

In contrast to a narrowing of the excitonic PL bands with a decrease in temperature typically reported for "conventional" binary NCs like CdSe or PbS,[42–44,46,47] both AIS/ZnS and HIS/ZnS show a steady growth of the PL FWHM, reaching ≈150 meV for AIS/ZnS and more than 200 meV for HIS/ZnS as the temperature is decreased down to 50 K [Fig. 4(c)]. Such traces can be quite naturally assumed to originate from temperature dependences of the energies of phonons participating in the radiative recombination of the self-trapped exciton and/or from temperature dependent electron-phonon interactions. At T < 50 K, both NC types display

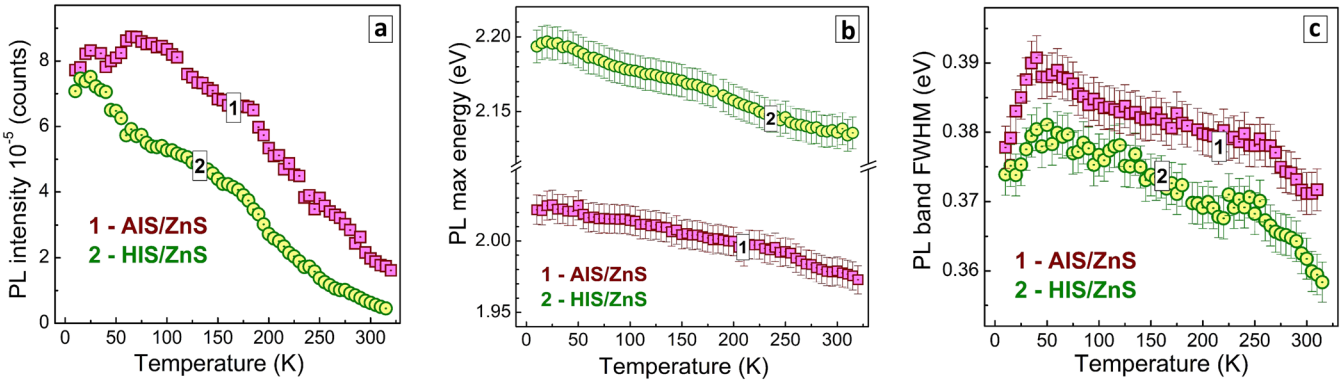

FIG. 4. Integral PL intensity (a), PL maximum (b), and PL FWHM (c) of AIS/ZnS NCs (curves 1) and HIS/ZnS NCs (curves 2) as a function of temperature.

a FWHM decrease as expected. This behavior may be accounted for by several possible recombination routes existing in this temperature window, for example, several types of self-trapped excitons responsible for several overlapping emission bands. The core-only AIS NCs show no particular temperature dependence of the PL FWHM [supplementary material, Fig. S10(c), curve 1], while HIS NCs display a complex behavior (curve 2), which is still to be interpreted in detail. We should also note that the samples for the low-temperature measurements show a lower room-temperature FWHM of the PL bands for all six samples (AIS, AIS/ZnS, CIS, CIS/ZnS, HIS, HIS/ZnS) as compared to the corresponding colloids. These differences can be attributed to partial reabsorption of the PL in the relatively thick layers of NCs on glass produced by drop-casting of concentrated colloids and used as samples for the low-T measurements.

4. Phonon spectra of HIS (HIS/ZnS) NCs

Based on the similarity of the XRD patterns of the HIS NCs under study and the previously studied AIS and CIS NCs, one can assume the same type of the crystalline structure for these materials. Additional confirmation of this assumption was obtained from the phonon spectra, studied by FTIR and Raman spectroscopies. The relatively strong PL of both core and core/shell NCs prevents direct studies of colloidal solutions with Raman spectroscopy and, therefore, an efficient electron acceptor, methyl viologen (MV^{2+}) chloride, was added to the solution to quench the PL. An almost complete PL quenching of all samples studied can be observed at a molar MIS/MV^{2+} ratio of 1–10 (M = Ag, Cu, Hg) as well as the presence of characteristic features of the MV cation radical in the Raman spectra [see Fig. 5(b)], indicating a photoinduced electron transfer from the NCs to MV^{2+} to be responsible for the PL quenching.

The phonon absorption spectrum of HIS NCs reveals at least three maxima, at 220, 278, and 335 cm^{-1}, respectively [Fig. 5(a)]. Although less structured, the Raman spectrum contains the main phonon features in the same frequency range, namely, 200–350 cm^{-1} [Fig. 5(b)]. Except for the frequency positions of the above features, the line shape of the IR phonon spectrum is similar for HIS and AIS NCs [Fig. 5(a)], confirming the similarity of their crystal structure, derived above from the XRD data.

The Raman spectrum of HIS NCs is distinct from the well structured spectrum of $CuInS_2$ NCs reported earlier.[48] The reason could be the small size and lower crystallinity of the present HIS NCs obtained in mild conditions. Nevertheless, for small AIS NCs (4 nm) synthesized at similarly mild conditions,[24] several peaks could still be distinguished in the Raman spectrum, with the strongest being found at about 290 cm^{-1} and weaker features at 240 and 345 cm^{-1} [Fig. 5(b)]. The larger broadening of the phonon Raman spectra of HIS NCs compared to similar AIS NCs may be explained by the fact that the Raman active vibrational modes are more sensitive to the kind of structural disorder that occurs in HIS NCs and that is manifested in the larger Urbach energy and broader XRD peaks.

One more striking similarity between the phonon spectra of all three kinds of core/shell NCs should be mentioned here (supplementary material, Fig. S11). This similarity confirms the similar effect of Zn assumed in Secs. III C 1 and III C 2 on the structure of the NC, in particular the formation of similarly alloyed NCs. The distinct peaks at 250 and 338 cm^{-1} are revealed in the IR spectra of HIS/ZnS NCs [Fig. 5(a)] at frequencies close to the other two core/shell systems (supplementary material, Fig. S11). The 338 cm^{-1} band could be the 335 cm^{-1} feature of the bare HIS NCs, shifted to higher frequencies by shell-induced strain and Zn-alloying. Earlier, we have observed by IR and Raman spectroscopies the development of strain in CdSe cores, induced by the lattice mismatch with, e.g., a CdS shell.[49] Even though the IR spectra of core/shell NCs are usually dominated by the TO (transverse optical) and SO (surface optical) phonons of the shell (and probably of the core/shell interface[50]), the phonon of the core can still be detected.[50] On the other hand, the feature at 338 cm^{-1} matches well the range of a SO phonon reported for ZnS NCs.[51,52] Moreover, in the spectrum of our HIS/ZnS NCs, the rest of the HIS modes (particularly at 220 and 278 cm^{-1}) is absent; instead, one mode at 250 cm^{-1} is observed [Fig. 5(a)]. Even though the latter peak is below the TO mode (the lowest optical frequency) of the ZnS NCs (≈275 cm^{-1}), it can be a hybrid interface mode of these NCs, further modified by interdiffusion. Strong additional proof favoring the assignment of both the 250 and the

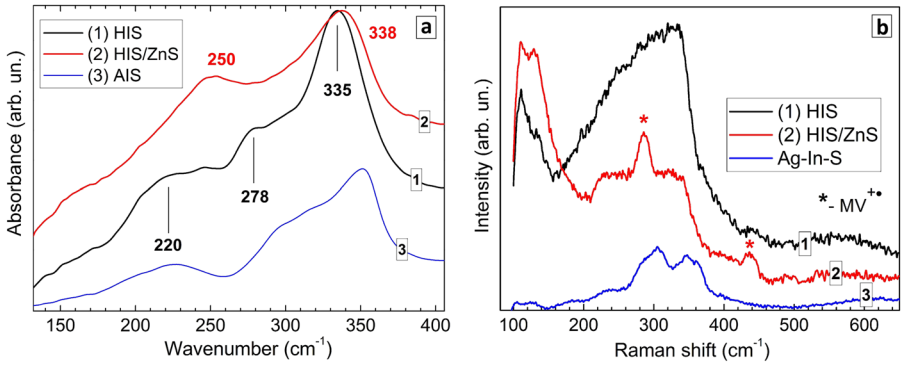

FIG. 5. IR (a) and Raman (b) phonon spectra of HIS, HIS/ZnS, and AIS NCs.

338 cm^{-1} IR peaks of the HIS/ZnS NCs to an (alloyed) shell and an interface is the observation of very similar spectra for the similarly synthesized AIS/ZnS and CIS/ZnS NCs (supplementary material, Fig. S11), despite noticeable differences between the spectra of core-only NCs [Fig. 5(b)].

In previous work on II-VI core/shell NCs[49,50] and more complex $CuInS_2$/ZnS, Zn–Cu–In–S, and Zn–Cu–In–S/ZnS NCs,[53,54] resonant Raman scattering has been proven to allow us to distinguish between pure and alloyed NC shells. In particular, the detection of ZnS-shell-related phonons in the Raman spectra was possible only using UV excitation, namely, 325 nm,[53] which is resonant with the shell transitions.[55] In the corresponding spectra of HIS/ZnS and AIS/ZnS NCs, no distinct LO (longitudinal optical) phonon peaks were observed under UV excitation but only asymmetrically broadened features in the same frequency range as for the corresponding core NCs [supplementary material, Fig. S8(b)]. Some redistribution of the scattering intensity toward the higher frequency side of the band can be explained by more probable contributions of the Zn–S bonds from the Zn-rich part of the alloyed shell at this excitation wavelength. This observation further confirms the above assumptions about the alloyed structure of the HIS/ZnS core/shell NCs and their similarity to the structures of AIS/ZnS NCs.

IV. CONCLUSIONS

We introduce a general synthesis of aqueous GSH-capped ternary AIS, CIS, and HIS NCs as well as corresponding core/shell NCs with zinc sulfide shells. The method allows for a broad variation of the NC compositions and sizes with applying size-selective precipitation as discussed for the case of AIS NCs in detail elsewhere.[12,21] This enables comparisons of the spectral properties of all three compounds with other properties remaining identical (dispersing medium, ligand, ratio of components, size, etc.). The HIS NCs display the same structural motif as the previously studied tetragonal chalcopyrite CIS and AIS NCs, which, in combination with the evidence collected by XPS, suggest that the most probable oxidation state of mercury in the HIS and HIS/ZnS NCs is +1. Such chalcopyrite Hg–In–S compounds seem not to be reported yet, neither as bulk crystals nor in the nanocrystalline form.

All three compounds manifest broadband PL with spectral widths larger than 400 meV centered in the visible spectra range. As in the case of AIS and CIS NCs reported earlier, the aqueous colloidal HIS (HIS/ZnS) NCs show little variations of the PL band FWHM upon size selection, temperature variation in the broad range of 10–350 K, deposition of a ZnS shell, or postsynthesis annealing. This can be regarded as an indication of a general PL mechanism in all three ternary compounds, which involves radiative recombinations of self-trapped excitons as the most plausible origin of the broadband light emission.

Raman phonon spectra of tetragonal HIS and HIS/ZnS NCs were reported for the first time, showing strong similarities with the Raman spectra of both AIS and CIS-based compounds and providing support for the assumed alloyed core/shell structure of HIS/ZnS NCs.

The reported synthetic approach allows detailed comparative studies of the three ternary compounds to be performed, maintaining as many as possible parameters of the NCs identical. Comparative investigations of the properties of the size-selected NC fractions, such as size- and composition-dependent dynamics of the PL decay and photoinduced electron transfer to acceptor substrates (such as methyl viologen), the behavior of CIS, AIS, and HIS NCs as spectral sensitizers and components of photoelectrochemical solar cells, etc., are currently under way.

SUPPLEMENTARY MATERIAL

See supplementary material for details of the synthesis of ternary MIS (M = Hg, Cu, Ag) and related core/shell NCs; description of setups and spectrometers; sets of data on the bandgap and Urbach energy of HIS and HIS/ZnS NCs with a different mercury-to-indium ratio as well as HIS NCs subjected to a thermal treatment, results of the energy-dispersive X-ray spectroscopic (EDX) analysis of composition-selected HIS NCs, and XRD peak positions and FWHMs as well as sizes of MIS and MIS/ZnS NCs; absorption and PL spectra of composition-selected HIS/ZnS NCs; hydrodynamic size distributions of HIS/ZnS NCs with a different nominal composition; XRD patterns of fresh and aged HIS/ZnS NCs; exemplary TEM and AFM images of HIS/ZnS NCs, X-ray photoelectron spectra of HIS/ZnS NCs in the ranges of Cu2p, Zn2p, C1s, and N1s electron binding energies; absorption and PL spectra of size-selected

HIS/ZnS NCs; temperature dependences of spectral PL parameters of HIS and AIS NCs; and IR phonon spectra and Raman spectra (excited at 325 nm) of MIS/ZnS NCs.

ACKNOWLEDGMENTS

This work was funded by the Volkswagen Foundation (Trilat project "New functionalities of semiconductor nanocrystals by controllable coupling to molecules"). D.S. acknowledges financial support from ESF Nachwuchsforschergruppe "E-PISA," 100310500. A.E. and N.G. thank German Science Foundation (DFG) for the partial support under Grant No. EY16/14-3.

The authors declare no competing financial interest.

REFERENCES

[1] D. Aldakov, A. Lefrançois, and P. Reiss, J. Mater. Chem. C **1**, 3756 (2013).
[2] S. V. Kershaw, A. S. Susha, and A. L. Rogach, Chem. Soc. Rev. **42**, 3033 (2013).
[3] K. E. Knowles, K. H. Hartstein, T. B. Kilburn, A. Marchioro, H. D. Nelson, P. J. Whitham, and D. R. Gamelin, Chem. Rev. **116**, 10820 (2016).
[4] S. R. Thomas, C. W. Chen, M. Date, Y. C. Wang, H. W. Tsai, Z. M. Wang, and Y. L. Chueh, RSC Adv. **6**, 60643 (2016).
[5] M. Sandroni, K. D. Wegner, D. Aldakov, and P. Reiss, ACS Energy Lett. **2**, 1076 (2017).
[6] W. M. Girma, M. Z. Fahmi, A. Permadi, M. A. Abate, and J. Y. Chang, J. Mater. Chem. B **5**, 6193 (2017).
[7] B. Chen, N. Pradhan, and H. Zhong, J. Phys. Chem. Lett. **9**, 435 (2018).
[8] O. Stroyuk, A. Raevskaya, and N. Gaponik, Chem. Soc. Rev. **47**, 5354 (2018).
[9] M. M. Chen, H. G. Xue, and S. P. Guo, Coord. Chem. Rev. **368**, 115 (2018).
[10] X. Bai, F. Purcell-Milton, and Y. K. Gun'ko, Nanomaterials **9**, 85 (2019).
[11] H. D. Nelson and D. R. Gamelin, J. Phys. Chem. C **122**, 18124 (2018).
[12] O. Stroyuk, A. Raevskaya, F. Spranger, O. Selyshchev, V. Dzhagan, S. Schulze, D. R. T. Zahn, and A. Eychmüller, J. Phys. Chem. C **122**, 13648 (2018).
[13] O. Stroyuk, F. Weigert, A. Raevskaya, F. Spranger, C. Würth, U. Resch-Genger, N. Gaponik, and D. R. T. Zahn, J. Phys. Chem. C **123**, 2632 (2019).
[14] H. Liu, C. Gu, W. Xiong, and M. Zhang, Sens. Actuators, B **209**, 670 (2015).
[15] C. Zhao, Z. Bai, X. Liu, Y. Zhang, B. Zou, and H. Zhong, ACS Appl. Mater. Interfaces **7**, 17623 (2015).
[16] W. W. Xiong, G. H. Yang, X. C. Wu, and J. J. Zhu, ACS Appl. Mater. Interfaces **5**, 8210 (2013).
[17] G. Gedda, G. R. Chen, Y. Y. Yao, W. M. Girma, J. D. Li, C. L. Yen, Y. C. Ling, and J. Y. Chang, New J. Chem. **41**, 14161 (2017).
[18] Z. Luo, H. Zhang, J. Huang, and X. Zhong, J. Colloid Interface Sci. **377**, 27 (2012).
[19] W. W. Xiong, G. H. Yang, X. C. Wu, and J. J. Zhu, J. Mater. Chem. B **1**, 4160 (2013).
[20] D. Deng, J. Cao, L. Qu, S. Achilefu, and Y. Gu, Phys. Chem. Chem. Phys. **15**, 5078 (2013).
[21] A. Raevskaya, V. Lesnyak, D. Haubold, V. Dzhagan, O. Stroyuk, N. Gaponik, D. R. T. Zahn, and A. Eychmüller, J. Phys. Chem. C **121**, 9032 (2017).
[22] A. Raevskaya, O. Rozovik, A. Novikova, O. Selyshchev, O. Stroyuk, V. Dzhagan, I. Goryacheva, N. Gaponik, D. R. T. Zahn, and A. Eychmüller, RSC Adv. **8**, 7550 (2018).
[23] A. Raevskaya, O. Rosovik, A. Kozytskiy, O. Stroyuk, V. Dzhagan, and D. R. T. Zahn, RSC Adv. **6**, 100145 (2016).
[24] A. E. Raevskaya, M. V. Ivanchenko, O. L. Stroyuk, S. Ya. Kuchmiy, and V. F. Plyusnin, J. Nanopart. Res. **17**, 135 (2015).
[25] R. D. Shannon, Acta Crystallogr., Sect. A: Found. Adv. **32**, 751 (1976).
[26] H. Hahn and W. Klingler, Z. Anorg. Allg. Chem. **263**, 177 (1950).
[27] M. Wakaki, Jpn. J. Appl. Phys., Part 1 **24**, 1471 (1985).
[28] J. A. Beun, R. Nitsche, and M. Lichtensteiger, Physica **26**, 647 (1960).
[29] J. A. Beun, R. Nitsche, and M. Lichtensteiger, Physica **27**, 448 (1961).
[30] G. Attolini, M. Curti, C. Paorici, C. Razzetti, and L. Zanotti, J. Crystal Growth **79**, 399 (1986).
[31] A. V. Naumkin, A. Kraut-Vass, and S. W. Gaarenstroom, NIST X-ray Photoelectron Spectroscopy Database, NIST, Standard Reference Database 20, Version 4.1, 2012.
[32] C. D. Wagner, W. M. Riggs, L. E. Davis, J. F. Moulder, and G. E. Muilenberg, *Handbook of X-Ray Photoelectron Spectroscopy* (Perkin-Elmer Corporation, Physical Electronics Division, Eden Prairie, MN, 1979).
[33] M. Yousaf, M. A. Saeed, A. R. Mat Isa, H. A. Rahnamaye Aliabad, and M. R. Sahar, Chin. Phys. Lett. **30**, 077402 (2013).
[34] J. S. Brinen and J. E. McClure, Anal. Lett. **5**, 737 (1972).
[35] V. I. Nefedov, Y. V. Salyn, P. M. Solozhenkin, and G. Y. Pulatov, Surf. Interface Anal. **2**, 170 (1980).
[36] C. Zylberajch-Antoine, A. Barraud, H. Roulet, and G. Dufour, Appl. Surf. Sci. **52**, 323 (1991).
[37] V. I. Nefedov, Y. V. Salyn, and X. Z. Keller, Neorg. Khimii **24**, 2564 (1979).
[38] R. Scheer and H. J. Lewerenz, J. Vac. Sci. Technol., A **12**, 56 (1994).
[39] A. E. Raevskaya, O. L. Stroyuk, S. Ya. Kuchmiy, and A. I. Kryukov, J. Mol. Catal. A: Chem. **212**, 259 (2004).
[40] O. L. Stroyuk, S. Ya. Kuchmiy, A. I. Kryukov, and V. D. Pokhodenko, *Semiconductor Catalysis and Photocatalysis on the Nanoscale* (Nova Science Publishers, Inc., New York, 2010).
[41] O. Stroyuk, V. Dzhagan, A. Raevskaya, F. Spranger, N. Gaponik, and D. R. T. Zahn, J. Lumin. **215**, 116630 (2019).
[42] S. Santhi, E. Bernstein, and F. Paille, J. Lumin. **117**, 101 (2006).
[43] L. Turyanska, A. Patanè, M. Henini, B. Hennequin, and N. R. Thomas, Appl. Phys. Lett. **90**, 101913 (2007).
[44] Y. Hamanaka, T. Ogawa, and M. Tsuzuki, J. Phys. Chem. C **115**, 1786 (2011).
[45] A. Yu. Kobitski, K. S. Zhuravlev, H. P. Wagner, and D. R. T. Zahn, Phys. Rev. B **63**, 115423 (2001).
[46] A. Eychmüller, A. Hässelbarth, L. Katsikas, and H. Weller, Ber. Bunsengesellschaft Phys. Chem. **95**, 79 (1991).
[47] J. Mooney, M. M. Krause, J. I. Saari, and P. Kambhampati, Phys. Rev. B **87**, 081201 (2013).
[48] V. M. Dzhagan, A. P. Litvinchuk, M. Y. Valakh, M. Kruszynska, J. Kolny-Olesiak, C. Himcinschi *et al.*, Phys. Status Solidi (a) **211**, 195 (2014).
[49] V. M. Dzhagan, M. Y. Valakh, A. G. Milekhin, N. A. Yeryukov, D. R. T. Zahn, E. Cassette *et al.*, J. Phys. Chem. C **117**, 18225 (2013).
[50] V. M. Dzhagan, Y. M. Azhniuk, A. G. Milekhin, and D. R. T. Zahn, J. Phys. D: Appl. Phys. **51**, 503001 (2018).
[51] A. Milekhin, L. Sveshnikova, T. Duda, N. Surovtsev, S. Adichtchev, L. Ding *et al.*, J. Vac. Sci. Technol., B **28**, C5E22 (2010).
[52] A. G. Milekhin, L. L. Sveshnikova, S. M. Repinski, and A. K. Gutakovski, Phys. Solid State **44**, 1976 (2002).
[53] V. Dzhagan, B. Kempken, M. Valakh, J. Parisi, J. Kolny-Olesiak, and D. R. T. Zahn, Appl. Surf. Sci. **395**, 24 (2017).
[54] J. Li, B. Kempken, V. Dzhagan, D. R. T. Zahn, J. Grzelak, S. Mackowski *et al.*, CrystEngComm **17**, 5634 (2015).
[55] A. G. Milekhin, N. A. Yeryukov, L. L. Sveshnikova, T. A. Duda, C. Himcinschi, E. I. Zenkevich *et al.*, Appl. Phys. A **107**, 275 (2012).